Lawrence Berkeley National Laboratory
Recent Work

Title

Revealing Molecular Mechanisms in Hierarchical Nanoporous Carbon via Nuclear Magnetic Resonance

Authors

Mao, H
Tang, J
Xu, J
et al.

Revealing Molecular Mechanisms in Hierarchical Nanoporous Carbon by

Nuclear Magnetic Resonance

Haiyan Mao[1†], Jing Tang[2,7†], Jun Xu[1], Yucan Peng[2], Jun Chen[2], Bing Wu[1], Yuanwen Jiang[4], Kaipeng Hou[3], Shuo Chen[5], Jiangyan Wang[2], Hye Ryoung Lee[2], David M. Halat[1,6], Bing Zhang[3], Wei Chen[2], Ariel Z Plantz[1], Zhiyi Lu[2], Yi Cui[2,7*] and Jeffrey A. Reimer[1,6*]

[1]Department of Chemical and Biomolecular Engineering, University of California, Berkeley, California, 94720, USA.

[2]Department of Materials Science and Engineering, Stanford University, Stanford, California, 94305, USA.

[3]Department of Chemistry, University of California, Berkeley, California, 94720, USA.

[4]Department of Chemical Engineering, Stanford University, Stanford, California, 94305, USA.

[5]Department of Physics, University of California, Berkeley, California, 94720, USA.

[6]Materials Science Division, Lawrence Berkeley Laboratory, Berkeley, California, 94720, USA.

[7]Stanford Institute for Materials and Energy Sciences, SLAC National Accelerator Laboratory, 2575 Sand Hill Road, Menlo Park, California, 94025, USA.

19   † Haiyan Mao and Jing Tang contributed equally to this work

20   *Correspondence and requests for materials should be addressed to **Yi Cui (yicui@stanford.edu) (Y.C.);**

21   **Jeffrey A. Reimer reimer@berkeley.edu (J.A.R.)**.

Summary

Hierarchical nanoporous carbons (HNC) have been proven to be an effective, sustainable and efficient adsorbent for the adsorption of volatile organic compounds (VOCs) and CO_2, although questions remain regarding the hierarchical structure regulation, and the adsorption mechanisms of adsorbate uptake and interactions within the HNC. Herein, we synthesize a honeycomb structured HNC from wood using a microwave-induced heating method incorporating K_2CO_3 activation. There materials are shown to exhibit Murray's Law multi-scale structures with micro- and mesopores, prompting a molecular scale study of adsorbate adsorption using nuclear magnetic resonance (NMR). NMR chemical shifts are consistent with ring current effects from the adsorbent, and integrated intensities are readily converted to mass-of-adsorbate per mass-of-adsorbent, providing a convenient and fast way to quantitate adsorption of adsorbate in HNC. Vapor phase VOCs adsorption results show NMR chemical shift changes with time after adsorption, suggesting initial adsorption into mesopores, followed by diffusion into micropores with increasing adsorption time. Persistent differences in observed shifts for adsorbed liquid vis-à-vis vapor phase in these HNC demonstrate of Schroeder's Paradox. These HNC also show high CO_2 adsorption capacity (4.3 mmol g^{-1} at 298 K and 1 bar) portending applications to carbon capture.

Introduction

Volatile organic compounds (VOCs) are common air pollutants contributing to the formation of ground-level ozone and carcinogens, known to be harmful to human health[1]. Carbon dioxide (CO_2) is the primary anthropogenic source of greenhouse gases that has impacted the earth's biosphere, especially climate change[2]. The rational design of renewable, multidimensional and microscopic materials for the adsorption of VOCs and CO_2 is therefore an important objective in functional materials research[1,3,4]. In particular, porous materials with nanosized pores play important roles in the science and technology of VOCs and CO_2 adsorption and separation[5,6].Nanoporous carbons derived from biomass are particularly promising due to their cost-efficient scalable fabrication, sustainable sourcing, high surface area and microporous dominated structure[7,8,9]. Typically, adsorption in such nanoporous carbon is determined by physical adsorption (via van der Waals forces) and ultimately micropore filling and capillary condensation[10,11]. Mesopores play an important role by providing transport channels for the adsorption and desorption of molecules, as well as further adsorption sites[12,13]. We therefore focus our attention on VOC and CO_2 adsorption within sustainable manufacturable[14] and hierarchically structured nanoporous carbons that exhibit a panoply of pore sizes.

Various synthetic methods have been proposed and developed for hierarchically nanoporous carbons (HNC), but many methods suffer from lack of structural control, harsh synthesis conditions, poorly degrading scaffolds and unsuitable pores (e.g. clogged pores and beaded holes)[15,16,17,18]. Inspired by plant structures, so-called Murray's Law materials have garnered attention recently owing to the ability to regulate pore diameters from macroscopic to microscopic dimentions[19,20]. Nevertheless, progress in

57 synthesizing Murray's Law materials remains slow, hindered by the ever-present bottleneck issues within

58 the interconnected pores. Herein we synthesize HNC derived from pinewood that follows Murray's Law

59 of interconnected micro- and mesopores using an innovative microwave-induced method incorporating

60 K_2CO_3 activation[21,22] (**Figure 1a**).

61   Several characterization methods have been used to investigate the adsorption performance of HNC,

62 such as adsorption capacity measurements via breakthrough experiments and gas adsorption

63 isotherms[23,24,25,26]. The interactions between adsorbed molecules and the carbon pores are important factors

64 during adsorption process and cannot be revealed by bulk methods[27]. Solid-state nuclear magnetic

65 resonance (SSNMR), however, is well suited to probe both local microscopic structure and the dynamical

66 properties of guest compounds confined in hierarchical porous carbons[28,29]. To date, NMR has been

67 utilized to probe the environment of adsorbed molecules onto host porous carbon-based materials[26] with

68 applications to supercapacitors[29,30], adsorption[30], and hydrogen storage[31]materials. These studies led us to

69 investigate hierarchical carbon materials by employing a combination of proton NMR and adsorption

70 isotherm measurements.

71   We compare solid-state NMR studies of three typical liquid and gaseous VOCs adsorbates: acetone,

72 toluene and *n*-hexane, as well as carbon dioxide. These molecules were chosen because they are

73 representative of environmental adsorption technologies and each molecule possesses different

74 dimensions and polarity. We observe that the adsorption of the VOCs from the liquid phase reflects

75 uptake into the mesopores of the hierarchical nanoporous carbons; in all adsorbates the resulting

76 chemicals shifts show the effects of polyaromatic ring currents from the carbon adsorbent. Integrating the

77 NMR signals from liquid-adsorbed VOCs yields uptakes of VOC mass that compare favorably to those

78 determined by adsorption experiments. We found that the observed NMR chemical shifts of VOCs

79 obtained by gas-phase and liquid-phase exposure are not the same, an apparent manifestation of

80 Schroeder's Paradox[32]. Finally, carbon dioxide physisorbs into HNC with a surprising capacity. Together,

81 these findings offered detailed insights into the interactions between liquid/gaseous adsorbates and

82 hierarchical nanoporous carbons via NMR.

83 **Results and Discussion**

84 **Physicochemical and structural characteristics**

85 The argon adsorption-desorption isotherm at 77 K of HNC is demonstrated in **Figure 1b**, and **Table S1**.

86 After microwave heating and K_2CO_3 activation, we observe that at relative pressure (P/P$_0$) below 0.05, the

87 nitrogen uptake increases sharply with the increase in relative pressure, proving the existence of

88 micropore structure. These adsorption isotherms are close to type a I-IV hybrid shape as defined by the

89 BBDT classification[33].

90   The specific surface area BET and total pore volume of our HNC after the K_2CO_3/microwave

91 treatment were remarkably improved (**Table S1**). The micropore surface area and volume significantly

92 increased from 30 to 1857 m^2/g, with the micropore volume of biochar increasing from 0.016 to 0.741 cc/

93 g, indicating that the micropores were developed in the mesopore walls while some mesoporous channels

94 collapse. The development of porosity is associated with the reaction of K_2CO_3 and C leading to the

95 formation of K_2O, K, CO, and CO_2 where the high microwave temperature is assumed to accelerate the

96   activation reaction[34]. The potassium species formed during the activation step diffuse into the internal

97   structure of the biochar matrix, which is presumed to widen existing pores as well as to create new ones.

98   Consequently, the presence of K_2CO_3 promotes the formation of dominant micropores and a small

99   fraction of mesopores, a much larger surface area, as well as a larger pore volume. The measured surface

100   areas are 3.4 times higher than those of carbons activated by K_2CO_3 via thermal heating of samples

101   derived from tobacco stem[35].

102   The pore size distribution curves plotted in **Figure 1c** are derived from argon adsorption

103   measurements using the Horváth-Kawazoe method[36] and indicate that the HNC manifest a wide pore size

104   distribution covering micropores (0.65-2 nm) and mesopores (2-50 nm). The overwhelming majority of

105   pore sizes include micropores (<2 nm), even supermicropores (0.7-2 nm) and even ultramicropores (<0.7

106   nm). Argon adsorption-desorption isotherms (**Figure 1c**) reveal a micropore distribution with a mean size

107   of 0.8 nm (D_{micro}); micropores within the HNC are elucidated via the low relative pressure region. The

108   K_2CO_3/microwave activated HNC thus appears to obey Murray's Law with three layers of structure at the

109   micro-/mesopore level as well as abundant interconnected pores. Such a super hierarchical pore structure

110   aids in the diffusion of adsorbates and is helpful to enhance the adsorption and desorption performance of

111   the HNC.

112   Transmission electron microscopy (TEM) image (**Figure 1d**) shows a disordered hierarchical

113   nanoporous structure containing mesopores. The large quantities of white spots between the disordered

114   carbon layers suggests that abundant mesopores exist in the hierarchical carbon from pinewood. To

115   observe wormhole-like pores as well as the interconnectivity of micropores and mesopores more clearly,

116 the real space images were transformed by an auto-threshold function to binary images (**Figure S1**). The

117 transformed image reveals that the micropores and mesopores are interconnected. Representative

118 scanning electron microscopes (SEM) image of HNC is depicted in **Figure 1e**, where notably the perfect

119 honeycomb structure and typically prismatic rectangular cells from the natural pinewood appear to be

120 maintained after chemical activation. These dimensions of the cells were ca. 20 μm and the wall thickness

121 was ca. 2 μm. It is important to note that there was no evidence of rupture of the pinewood pore walls,

122 indicating that the wall material had a high tensile strength such that K_2CO_3 could be impregnated and

123 dissolved K_2CO_3 could be removed. Upon K_2CO_3/microwave activation, the pores were etched and

124 developed during the reaction of K with carbon. These results are similar to previously published SEM

125 images of carbonized and activated virgin cork[37,38]. The present K_2CO_3/microwave activation of pinewood

126 yields an interconnected HNC obeying Murray's Law via a facile, low-cost, and environmentally friendly

127 process.

128 **Adsorption of liquid acetone in hierarchical nanoporous carbon**

129 Proton (^{1}H) spin-echo magic angle spinning (MAS) NMR spectra of acetone adsorbed onto hierarchical

130 nanoporous carbon for the range 23 wt % to 100 wt % loadings are shown in **Figure 2a**. Initial adsorption

131 gives rise to a broad signal at -2.5 ppm, shifted to low frequency from that for liquid acetone (2.2 ppm) by

132 4.7 ppm, which is assigned to the "in-pore" acetone (**Figure 2b**). This shift to lower frequency results

133 from ring currents emanating from the aromatic rings of the graphene planes in the pore walls[39]. This has

134 previously been confirmed experimentally and theoretically on microporous/mesoporous porous carbon[39].

135 The ring current effect is strongly dependent on the distance between the NMR-observed nucleus and the

136 center of the aromatic ring[40,41].

137   With the increase of acetone loading, the broad line grows in intensity until it reaches a plateau at

138 higher loadings (63 wt %), suggesting pore-filling and saturation. As the loading level increases further

139 to 82 wt %, a narrower peak appears at 2.1 ppm, a shift that is close to that of the methyl protons in neat

140 acetone. The peak is associated with liquid acetone external to the HNC pores, which is assigned to the

141 "ex-pore" acetone (**Figure 2b**). The chemical shift deviation between the in-pore resonance and neat

142 acetone is quantified by $\Delta\delta = \delta_{i-pore} - \delta_{neat}$, and has a value of -4.5 ppm here (corresponding to the two

143 peaks in **Figure 2a**).

144   To quantitate exchange between the in-pore and ex-pore enviroments[41], two-dimensional ^{1}H

145 homonuclear exchange experiments[42] were conducted at various mixing times (0.001, 0.1 and 0.25 s); the

146 results are shown in **Figure 2c to 2e**. As expected, the cross peaks appearing at mixing times in excess of

147 0.1 s confirm that acetone exhibits slow exchange between "in-pore" and "ex-pore" environments.

148 **Adsorption of liquid toluene and *n*-hexane in hierarchical nanoporous carbons**

149 The ^{1}H spin echo-MAS spectra of toluene and *n*-hexane adsorbed onto HNC as a function of loading are

150 in **Figure S2**. The qualitative features of these spectra are analogous to those observed from acetone; the

151 methyl and aromatic proton resonances from toluene reveal in-pore and ex-pore environments, as do the

152 CH_3 and CH_2 resonances from *n*-hexane. At a mass ratio of 62 wt % the pores of HNC become "full" and

153 the toluene/*n*-hexane loading reaches saturation. As the loading increases further the narrow lines

154 emanating from ex-pore features become prominent. Therefore, the four peaks at low and high

155 frequencies are assigned to in- and ex-pore toluene respectively (**Figure S2a**). For these adsorbates, we

156 calculate Δδ to be -4.2 ppm (acetone), -4.2 ppm (toluene) and -4.4 ppm (both CH_3 and CH_2 resonances

157 from *n*-hexane (**Figure S2b**). The chemical shift deviations Δδ are very similar for the three adsorbates,

158 indicating that the underlying mechanism is mainly due to ring-current shifts associated with the aromatic

159 rings in the HNC.

Comparison of uptakes between NMR spectra and adsorption isotherms

161 Quantitative NMR spectroscopy can be used to provide an alternative method for obtaining adsorption

162 uptakes[43]. The adsorption isotherms of acetone/toluene/*n*-hexane for our HNC were acquired using a

163 sorption analyzer at 298 K with N_2 as the carrier gas and are shown in **Figure 3c**. Proton (^{1}H) single-pulse

164 NMR spectra of liquid acetone, toluene and *n*-hexane spectra adsorbed at various loadings were

165 deconvoluted and integrated using the DMFit software[44] (**Figure S3**), thereby providing the amount in

166 mmol of adsorbed in-pore VOC per gram of HNC (**Figure 3c**). To compare NMR uptake to gas sorption

167 studies, the abscissa is given as mmol of VOC adsorbed: for the NMR data this is the amount of liquid

168 VOC placed into the sample, and for the isotherm data this is determined by converting the partial

169 pressure (P/P$_0$) to mmol via the Peng–Robinson equation of state[45]. The result shows that ultimate uptake

170 of adsorbates as measured from adsorption isotherms are in good agreement with those determined from

171 the NMR spectra. The reason for the lag at low uptakes is unclear and requires further studies.

172   The adsorption capacity of the three compounds within the HNC was found to be in the order of

173 toluene > acetone > *n*-hexane. This order of adsorption capacity clearly demonstrates the effects of

174 molecular dimension and polarity of these three VOCs[41,46]. By way of comparison with the HNC

175 synthesized in this work, VOC isotherms and adsorbate capacity on commercial activated carbon were

176 also performed. Our HNC exhibit higher adsorption capacities for all VOCs compared with commercial

177 activated carbon (**Figure S4**). The saturated toluene, acetone and *n*-hexane adsorption capacities reached

178 11.9, 8.8 and 6.8 mmol/g, respectively, which are 1.5, 1.6 and 1.9 times higher than those of commercial

179 activated carbon, respectively. Consequently, our HNC that demonstrates a high adsorptive performance

180 of VOCs provides a cost-effective alternative to commercial activated carbon in many air quality

181 remediation and treatment applications.

VOCs vapor adsorption in hierarchical nanoporous carbons

183 In many practical applications, VOC adsorption occurs from the vapor phase rather than the liquid phase

184 where the time required for adsorbents to equilibrate with dosed gas has significance for process swing

185 designs. Therefore, we have further examined vapor VOCs loaded onto HNC as a function of adsorption

186 time. **Figure 4b** depicts the ^{1}H NMR spectra of acetone vapor adsorbed onto HNC as a function of

187 adsorption time at room temperature. After exposure to acetone vapor (**Figure 4b**) for 1 min, a broad

188 peak at -0.4 ppm (labeled "A") is observed. With increasing adsorption time to 91 min, the intensity of

189 peak "A" gradually decreases and shifts upfield, ultimately disappearing after 150 minutes. A second,

190 upfield peak a (~2.5 ppm, "peak B") increases in intensity to a maximum intensity, suggesting of

191 saturation of the micropores. **Figure 4g** further confirms the total proton NMR signal integrated from the

192 "within pore" environments (both peak A and peak B) changes as a function of adsorption time where, as

193 expected, the adsorption uptake increases with time and reaches saturation at ~91 min. Compared to the

194 liquid-phase loaded HNC spectrum (**Figure 4a**), the ex-pore peak at ~2 ppm does not appear, indicating

195 that all the gas molecules enter into the pores and no extra molecules remain exterior to the pores.

196   Noting that adsorbate molecules in smaller pores experience a greater average degree of ring current

197 shielding and thus demonstrate a greater shift to low frequency than those in larger pores[30], the more

198 negative chemical shift for peak B suggests that these acetone molecules are adsorbed in smaller pores

199 vis-á-vis those corresponding to peak A. We consider two hypotheses to explain the NMR spectra shown

200 in **Figure 4c to 4g**. First, diffusion of acetone within the HNC pore network over time could change the

201 observed NMR shifts as the adsorbate molecules diffuse to differing carbon-pore environments (**Figure**

202 **4c**). To test this hypothesis, we performed a ^{1}H NMR experiment where acetone vapor was exposed to

203 HNC for 1 minute, and then a further 3 hours of exposure to N_2 gas for diffusion/equilibration. **Figure S5**

204 shows that the chemical shift of the spectrum is not changed after waiting for 3 hours. Additionally, we

205 conducted a ^{1}H NMR experiment where acetone vapor was exposed to HNC for 1 minute, followed by

206 heating the acetone- adsorbed samples to 55 $^\circ$C for 30 min and then cooling down to room temperature.

207 **Figure S6** shows that the chemical shift of the spectrum is unchanged after the treatment. Therefore, the

208 changes in **Figure 4b** are unlikely to be due to the acetone diffusion over time within the HNC.

209   A second hypothesis is that thermodynamic effects are responsible for the observed NMR behavior.

210 Schroeder's Paradox[32], wherein adsorption of saturated vapor differs from that when exposed to liquid,

211 has been reported and discussed extensively in the literature[47,48]. Schroeder's Paradox occurs in strongly

212 interacting systems, in which the materials undergo a high degree of swelling[48]. The data shown in **Figure**

213 **4b** suggest that the distribution of acetone in HNC mesopores depends upon the way in which the

214   adsorbate was introduced, and that neither time nor modest temperature annealing redistribute the

215   adsorbed acetone molecules so as to yield the same molecular environments. **Figure 4d-4g** interpret the

216   manifestation of Schroeder's Paradox in the aspect of differences in chemical shifts **(Figure 4e)** and

217   adsorption capacities (Figure 4f and 4g) for liquid and gaseous acetone. **Table S3** displays spectral

218   simulation parameters of Gaussian/Lorentzian of liquid and vapor VOCs obtained from deconvolution

219   using the DMfit software. We summarize the adsorption capacities of HNC for all VOCs after liquid and

220   vapor exposure in **Table S4**. It is clear that the adsorption capacity of saturated VOCs within the HNC is

221   quite different between saturated liquid and vapor VOC; for example, the adsorption capacity of 11.8

222   mmol/g for acetone vapor with exposure time of 150 min is quite different from that of liquid acetone

223   with 8.8 mmol/g at 141 wt % loading (**Figure 4f and 4g**). This difference of adsorption capacities would

224   seem to be an *adsorbate-probed* manifestation of Schroeder's Paradox.

225   The observed chemical shifts of adsorbed acetone from the liquid phase are different from those

226   arising from vapor-phase adsorbed acetone (**Figure 4e**). This might be rationalized assuming that the

227   acetone vapor diffuses into the pore structure in a different way than that of liquid acetone. A comparison

228   of effective liquid and vapor diffusion time (**Figure 2a and Figure 4b**) in HNC reveals that acetone vapor

229   requires a longer period (150 min) to diffuse from mesopores to reside in microporous environments, as

230   confirmed by the large nucleus-independent chemical shifts (NICS) value obtained at that time. After 16

231   minutes, two peaks are clearly present, revealing that mesopores and micropores are filled with acetone

232   molecules, which do not undergo exchange on the NMR time scale, thus indicating that slow diffusion in

233   HNC (**Figure 2c to 2e**). However, liquid acetone diffuses immediately into the micropores (**Figure 2a, 23**

234   **wt %**) and fills the mesopores at higher loading (**Figure 2a, 63 wt %**), in addition to causing spectral

235   broadening spectra at -2.5 ppm (**Figure 4e**), emphasizing that limited diffusion occurs on the NMR time

236   scales.

237   **Figure 5b** presents the ^{1}H NMR spectra of HNC subjected to vapor-phase toluene as a function of

238   adsorption time. After toluene exposure for 1 min, several peaks appear. Those with the largest shifts are

239   easily assigned to ex-pore aromatic and ex-pore methyl protons owing to the similarity of their shifts to

240   those of neat toluene, consistent with a picture in which some toluene molecules are not able to go into

241   the pores after short exposure times because the molecular size of toluene is larger than that of the narrow

242   pores in the HNC. Assignment of the upfield shifts proton peaks is not clear, yet the shifts suggest ring

243   current effects and thus we assign them to in-mesopore (C-H) and in-mesopore CH$_3$, as indicated in

244   **Figure 5b** (the spectrum at 1 min). With an increase in adsorption time (150 minutes) the two broad

245   peaks at 1.28 and -0.68 ppm shift further upfield (i.e., lower chemical shift values) to -2.74 and -3.85

246   ppm. Again, the increased ring current effects are the likely cause, and thus we assign these peaks to the

247   in-micropore (C-H) and in-micropore (CH$_3$), respectively. Interestingly, for the spectrum of vapor

248   adsorbed HNC at 150 min, the signal at 0.88 ppm assigned to in-mesopore (C-H) environments does not

249   move to lower chemical shift, indicating that there are toluene molecules still adsorbed in the mesopore

250   due to the larger molecule size of toluene, as compared to the narrow pore size of HNC. Compared to the

251   liquid adsorption spectrum at 100 wt % toluene (**Figure 5a** on the top), the vapor spectra provide more

252   subtle information about the interactions in different pores as a function of adsorption time. As in the case

253   of acetone, it would appear that Schroeder's Paradox is at play.

254   The ^{1}H NMR spectra obtained for vapor *n*-hexane vapor within the HNC as a function of adsorption

255   time are shown in **Figure 5d**. With the initial exposure to *n*-hexane for 1 min, ^{1}H MAS NMR signals of

256   the in-mesopore (CH_2) and in-mesopore (CH_3) molecules in the range of ~2 to ~-2 ppm overlap, while the

257   broad peak at -3.94 ppm emerges and is assigned to the in-micropore (CH_2 and CH_3) environments. At 6

258   min, the sharp peak at 1.98 pm is assigned to the overlaps of two environments corresponding to ex-pore

259   (CH_2) and ex-pore (CH_3). With increasing of adsorption time, as expected, in-mesopore (CH_2) and in-

260   mesopore (CH_3) signals diminish, while those at -3.71 ppm attributed to the in-micropore (CH_2 and CH_3)

261   increase. It is interesting to note that the chemical shift difference ($\Delta\delta$ = 0.6 ppm) between ex-pore *n*-

262   hexane vapor and ex-pore liquid *n*-hexane peaks (**Figure 5c**) is probably due to a small amount of

263   chemical exchange between the ex-pore and in-pore gas species, which shifts the chemical shift of the

264   vapor ex-pore vapor away from the liquid ex-pore[31]. As also observed with acetone and toluene, the

265   nature of pore occupancy by the adsorbate depends on whether the sample is exposed to saturated vapor

266   or liquid.

CO$_2$ capture performance

267

268   **Figure 6a** shows the CO_2 adsorption isotherms for HNC at 298 K and 1 bar. Remarkably, it can be

269   found that our HNC exhibited a high CO_2 adsorption capacity of 4.3 mmol g^{-1}, thereby reflecting a

270   strongly competitive CO_2 adsorption capacity among the other porous framework materials (e.g., 3.78

271   mmol g^{-1} for rice husk derived activated carbons at 298 K and 1 bar[49]; for comparison the capacity of

272   MOF-74 at 298 K and 1 bar[50] is 4.1 mmol g^{-1}). The ^{13}C MAS NMR spectra of ^{13}CO$_2$-dosed HNC exhibit

273   resonances which were assigned to physisorbed CO_2 at 121.7 ppm (**Figure 6c**). A similar peak at 124.7

274 ppm was observed in MOF-274[44]. The -6 ppm chemical shift vis-à-vis free gas-phase CO_2 (127.7 ppm at

275 1 bar) is due to aromatic ring currents[51]. Thereby, our HNC has excellent CO_2 capacity that, combined

276 with the low-cost, sustainable, facile and up-scalable synthesis method warrants further study with

277 potential application towards carbon capture technologies.

278 **Conclusions**

279 In summary, we prepared hierarchical nanoporous carbons from pinewood that exhibits multi-branching

280 micro-and-mesopores and obeys Murray's Law. These HNC exhibit a large surface area (2765 m^2/g) and

281 micropore volume (0.741 cc/g), which portends a potentially important role in the adsorption of gases.

282 We probed the adsorption of VOCs at the molecular level via ^{1}H MAS NMR. Acetone, toluene and *n-*

283 hexane were found to exhibit NMR spectra that quantify the mass of adsorbate, and changes of the

284 spectra with time were seen after exposure to the HNC were observed. Liquid acetone, toluene, and *n-*

285 hexane present broad NMR signals that are shifted to lower frequency; these peaks are assigned to in-pore

286 adsorbed VOCs where the shift is attributable to the ring currents arising from the graphene-like sheets. In

287 addition, narrow signals at appear at the same chemical shift as those from the neat liquid VOCs. These

288 latter peaks appear only at high loadings, consistent with pore saturation. In the case of acetone

289 adsorption at high loadings, the adsorbate undergoes slow (~ 0.1 seconds) exchange between in-pore and

290 ex-pore environments. Uptakes determined from ^{1}H NMR are obtained by calibrating the signal at various

291 loadings, and are consistent with that of gas sorption analyzer data at saturation coverages, showing that

292 NMR allows for fast determination of the ultimate adsorption capacities of VOCs within the hierarchical

293   nanoporous carbons. Regarding gaseous adsorption, ^{1}H NMR spectra of vapor-adsorbed VOCs into HNC

294   as a function of exposure time showed that VOCs occupy both mesopores and micropores, and by

295   comparison to liquid adsorption, we proposed the data are consistent with an observation of Schroeder's

296   Paradox. In the case of gas phase uptake of CO_2 we find that the HNC show high physisorption of CO_2

297   (4.3 mmol g^{-1}), consistent with potential application to carbon capture technologies. We conclude that the

298   synthesis of hierarchical nanoporous carbons, and the NMR-determined pore distribution of adsorbates

299   with loading and time, portends the observation of both new phenomena and novel technological

300   applications in the multidisciplinary field of energy-environment-economics.

Experimental Procedures

301

302   **Synthesis of hierarchical nanoporous carbons**. The pinewood chips were thoroughly washed and

303   placed into a muffle furnace prior to carbonization. The carbonization temperature was 600 °C under a

304   purified N_2 flow (0.5 L/min). After carbonization, the char was sieved to obtain particles of 1~2 mm in

305   diameter. The char produced was mixed with K_2CO_3 with an impregnation K_2CO_3/char mass ratio of 3.

306   The mixture was heated in a modified 2.45 GHz microwave oven with an output power of 700 W for 20

307   min, with humidified N_2 as the carrier gas. The resultant hierarchical nanoporous carbon was washed with

308   0.1 M hydrochloric acid and rinsed repeatedly with hot and cold distilled water to remove residual K from

309   the surface of the sample until the filtrate reached neutral pH. The experimental setup is shown in **Figure**

310   **1a**. Additionally, to provide a comparison to the as-synthesized HNC, commercial activated carbons were

311   obtained from EM industries Inc. Industries Inc. and characterized in tandem as described below.

Sample characterization. Scanning electron microscopy (SEM) images were acquired on a Hitachi S-2500 (Tokyo, Japan) analytical scanning electron microscope using a beam energy of 20 kV and an In-Lens detector. TEM images were acquired on a ThemIS microscope (TEM 0.5) at 300 kV. The specific surface area and pore structure of the samples were evaluated using a Micromeritics ASAP2010 physical adsorption instrument at 77 K in liquid N_2. The specific surface area was estimated by the Brunauer-Emmett-Teller method[25]. The pore size distribution for micropores was calculated using the t-plot method. Powder X-ray diffraction (PXRD) measurements were carried out on a Rigaku MiniFLex 6G Benchtop X-ray powder diffractometer operating at 20 mA and 40 kV using Cu Kα_1 radiation (λ = 1.5406 Å) at room temperature.

Preparation of samples in NMR rotors for adsorption experiment. The schematic of preparation of samples was depicted in **Figure 3a.** The samples used herein were ground into powder (fine mesh) and placed into the vacuum oven at 120 °C overnight, then packed into 4 mm sealing cells, which were subsequently put into 4 mm outer diameter zirconia MAS rotors. Sealing cells were weighed prior to and after packing to determine the mass of the hierarchical nanoporous carbons. For liquid VOCs, a microsyringe was used to inject solvents (acetone (Sigma, 99 %), toluene (Sigma, 99.9 %), and *n*-hexane (Sigma, *n*-hexane 98.5 %)) into the sealing cell. The samples were subjected to NMR analysis 24 hours after adsorption in order to reach the adsorption equilibrium. The aforementioned above adsorption experiment was performed in the glove box with N_2 gas to avoid effects of moisture. The following mass balance equation was used to determine the used mass of VOCs injected into HNC:

$$W = \frac{W_2 - W_1}{W_1} \times 100\%$$

331 (1)

332 where W is the mass of VOCs normalized by the mass of the hierarchical nanoporous carbon material; W_2

333 is the weight of the HNC after adding VOCs; and W_1 is the weight of the HNC. Neat solvent experiments

334 were performed on a mixture of KBr and pure VOCs in the sealing cell to ensure rotor stability during

335 NMR. For gaseous adsorption, VOCs solvents and rotor with HNC were placed in separate scintillation

336 vials, then placed in a sealed vial; further details are given below and in **Figure 3a**. Adsorption isotherms

337 were measured by using the gas adsorption analyzer. After adsorption, the inserts with liquid/vapor VOC

338 adsorbed HNC were transferred into the vacuum oven at 120 °C, left overnight, and then were stored in a

339 desiccator for future use.

340 Prior to CO_2 adsorption, HNC samples were packed into a 3.2 mm rotor under nitrogen environment

341 to avoid moisture. The rotor containing samples was then put into a home-bult gas set up[44] (**Figure 6b**).

342 Before dosing $^{13}CO_2$ gas (Sigma-Aldrich, 99 atom % ^{13}C, <3 atom % ^{18}O), the samples were evacuated for

343 10 min. $^{13}CO_2$ dosing was carried out for overnight to reach the equilibration at room temperature (~298

344 K). Meanwhile, a gas gauge was used to control and record the pressure inside the samples. After

345 adsorption, the rotor was sealed by the cap using a moveable plunger inside the set up to avoid air and

346 moisture.

347 **NMR experiments.** The schematic of NMR experiments was shown in **Figure 3b.** The ^1H MAS

348 NMR spectra were measured at 500.12 MHz (11.7 T) on a Bruker Avance spectrometer with a Bruker

349 narrow bore H/C/N magic angle spinning (MAS) probe. The ^1H MAS one-pulse NMR spectra of VOCs

350   adsorption in hierarchical nanoporous carbon was acquired at a sample spinning rate of 8 kHz. Neat

351   VOCs with KBr were spun at 5 kHz. To eliminate the background signal from the NMR probe, both spin

352   echo ($90° − \tau − ¿ 180° − \tau − ¿$ acquire) and one-pulse sequence measurements were used to record the ^1H

353   spectra[52]. A radio-frequency (RF) field strength (B_1) of 60 kHz and a spin echo delay of $\tau = ¿$ 119 μs were

354   used, while using a recycle delay of 1 s. ^1H two-dimensional (2D) homonuclear exchange experiments

355   were performed on samples with VOCs loadings where additional peaks (relative to the neat VOCs)

356   emerged[53]. Mixing times in the range of 0.001 to 0.25 seconds were used. For CO_2 adsorption

357   experiments, the NMR experiment was performed at 16.4 T using a Bruker 3.2 mm MAS probe with a

358   MAS rate of 15 kHz. ^{13}C NMR spectra by direct excitation was measured in the CO_2 adsorption

359   experiment. The proton and ^{13}C peaks of adamantane at 1.85 and 38.5 (tertiary carbon – left-hand

360   resonance) ppm were used to as an external reference, respectively. All NMR experiments were

361   performed at ambient temperature (~298 K). Spectral fitting was carried out using DMfit software.

362   Deconvolutions were calculated using a mixture of Gaussian and Lorentzian lineshapes to describe the

363   different features in the spectra.

364   The ^1H MAS one-pulse NMR spectra of vapor VOCs adsorption in hierarchical nanoporous carbon

365   were also acquired at a sample spinning rate of 8 kHz. The schematic of vapor adsorption in HNC is

366   shown in **Figure S7**. HNC were packed into a 4 mm rotor in the N_2 glovebox. VOCs solvents and a rotor

367   with HNC were placed in separate scintillation vials, then both placed in a parafilm-sealed beaker. To

368   minimize moisture adsorption, this sealed beaker was placed in a glove box for various adsorption times.

369 After a specified adsorption time (e.g. 1 minute), the rotor was capped in the glove box and transferred to

370 the NMR spectrometer.

371   To assess the diffusion of acetone within the mesopores of the HNC, vapor acetone was exposed to

372 HNC for 1 minute in the sealed beaker, and then the rotor was quickly capped and placed in an Ar glove

373 box for 3 h. Additional ^{1}H NMR experiments were carried out as shown in **Figure S7**. Prior to acetone

374 vapor was exposed to HNC for 1 minute, argon gas was introduced to the glovebox and following by

375 evacuating for 2 h. Afterwards, the rotor cap quickly inserted and sealed, and then the sample was heated

376 to 55 $^\circ$C for 30 min in the oven. After cooling to room temperature, a one-pulse MAS NMR experiment

377 was performed.

378 **Adsorption isotherm experiments.** The adsorption isotherms were performed gravimetrically using a

379 sorption analyzer (TA Instruments, model VTI-SA) at 298 K with N_2 as the carrier gas. The system

380 recorded the equilibrium weight of the biomass based HNC in response to a step change in the

381 concentration of the adsorbate (relative pressure range of 0.01~0.9). Between 3~5mg of HNC powder was

382 weighed and placed into the container of the analyzer. Equilibrium was assumed to be reached when the

383 weight changed by less than 0.001 % in a 5 min period.

384 **Acknowledgements**

389   for Energy Storage Research, an Energy Innovation Hub funded by the US Department of Energy, Office

390   of Science, Basic Energy Science. We appreciate technical discussions with Dr. Alexander C. Forse and

391   Dr. Thomas M. Osborn Popp.

392   **Author Contributions**

393   H.M., J.T., Y.C., and J.A.R conceived the idea and composed the manuscript. H.M. and J.T. planned the

394   study, designed the experiment, analyzed the data. H.M. and J.T. performed all the experiments together

395   with the assistance of J. X. performed the 2D exchange NMR experiment. Y.C. and J.A.R. supervised the

396   project. All the authors reviewed and commented on the manuscript.

397   **Declaration of interests**

398   The authors declare no competing interests.

399   **Data availability**

400   The data that support the plots within this paper and other finding of this study are available from the

401   corresponding authors on request.

402
403   **References**

404   1.   Brüggemann, M., Hayeck, N. & George, C. (2018). Interfacial photochemistry at the ocean surface

405   is a global source of organic vapors and aerosols. Nat. Commun. 9, 2101.

406   2.   Boyd, P. G., Chidambaram, A., García-Díez, E., Ireland, C. P., Daff, T. D., Bounds, R., Gładysiak,

407   A., Schouwink, P., et al. (2019). Data-driven design of metal–organic frameworks for wet flue gas

408   CO_2 capture. Nature. 576, 253-256.

409   3.   Chen, W. Y., Jiang, X., Lai, S., Peroulis, D. and Stanciu, L. (2020). Nanohybrids of a MXene and

410   transition metal dichalcogenide for selective detection of volatile organic compounds. Nat.

411   Commun. 11, 1302.

412   4.   Dong, J. and Zhang, K. (2017). Ultrathin two-dimensional porous organic nanosheets with

413   molecular rotors for chemical sensing. Nat. Commun. 8, 1142.

414   5.   Chen, W., Chen, S., Liang, T., Zhang, Q., Fan, Z.,Yin, H., Huang, K., Zhang, X., Lai, Z., and

415   Sheng, P. (2018). High-flux water desalination with interfacial salt sieving effect in nanoporous

416   carbon composite membranes. Nat. Nanotechnol. 13, 345–350.

417   6.   McDonald, T. M., Mason, J. A., Kong, X., Bloch, E. D., Gygi, D., Dani, A., Crocella, V.,

418   Giordanino, F., Odoh, S. O., Drisdell, W.S. et al. (2015). Cooperative insertion of CO_2 in diamine-

419   appended metal-organic frameworks. Nature. 519, 303–308.

420   7.   Joo, W. J., Lee, J.H., Jang, Y., Kang, S.G., Kwon, Y.N., Chung J., Lee, S., Kim, C., Kim, T.H.,

421   Yang, C.W., et al. (2017). Realization of continuous Zachariasen carbon monolayer. Sci. Adv. 3,

422   1–9.

423   8.   Yadavalli, T., Ames, J., Agelidis, A., Suryawanshi, R. & Jaishankar, D. (2019). Drug-encapsulated

424   carbon (DECON): A novel platform for enhanced drug delivery. Sci. Adv. 1–13.

425   9.   Xu, L., Li,Y., Gao, S., Niu, Y., Liu, H., Mei, C., J., Cai, Xu, C. (2020). Preparation and properties

426   of cyanobacteria-based carbon quantum dots/polyvinyl alcohol/nanocellulose composite. Polymers

427   (Basel). 12, 1–12.

428   10.   Yu, D., Goh, K., Wang, H., Wei, L., Jiang, W., Zhang, Q., Dai, L., Chen, Y., (2014). Scalable

429   synthesis of hierarchically structured carbon nanotube-graphene fibres for capacitive energy

430   storage. Nat. Nanotechnol. 9, 555–562.

431   11.   Tseng, P., Napier, B., Zhao, S., Mitropoulos, A.N., Applegate, M. B., Marelli, B., Kaplan, D. L.,

432   Omenetto, F. G. (2017). Directed assembly of bio-inspired hierarchical materials with controlled

433   nanofibrillar architectures. Nat. Nanotechnol. 12, 474–480.

434   12.   Abraham, J., Vasu, K. S., Williams, C. D., Gopinadhan, K., Su, Y., T. C., Cherian, J. Dix, Prestat,

435   E., Haigh, S. J., Grigorieva, I. V., Carbone, P. (2017). Tunable sieving of ions using graphene

436   oxide membranes. Nat. Nanotechnol. 12, 546–550.

437   13.   Wu, J., Wu, J., Xu, F., Li, S., Ma, P., Zhang, X., Liu, Q., Fu, R., and Wu, D. (2019). Porous

438   polymers as multifunctional material platforms toward task-specific applications. Adv. Mater. 31,

439   1–45.

440   14.   Wang, H., Min, S., Ma, C., Liu, Z., Zhang, W., Wang, Q., Li, D., Li, Y., Turner, S., Han, Y., et al.

441   (2017). Synthesis of single-crystal-like nanoporous carbon membranes and their application in

442   overall water splitting. Nat. Commun. 8, 13592.

443   15.   Jessen, B. S., Gammelgaard, L., Thomsen, M. R., Mackenzie, D. M. A., Thomsen, J. D., Caridad,

444   J. M., Duegaard, E., Watanabe, K., Taniguchi, T., and Booth, T. J., et al. (2019). Lithographic band

445   structure engineering of graphene. Nat. Nanotechnol. 14.

446   16.   Xia, H., Tang, H., Zhou, B., Y., Li, X., Zhang, Shi, Z., Deng, L., Song, R., Li, L., Zhang, Z., and

447   Zhou, J. (2020). Mediator-free electron-transfer on patternable hierarchical meso/macro porous

448   bienzyme interface for highly-sensitive sweat glucose and surface electromyography monitoring.

449   Sensors Actuators, B Chem. 312, 12792.

450   17.   Lin, X. , Liang, Y., Lu, Z., Lou, H., Zhang, X., Liu, S., Zheng, B., Liu, R., Fu, R., and Wu D.

451   (2017). Mechanochemistry: A green, activation-free and top-down strategy to high-surface-area

452   carbon materials. ACS Sustain. Chem. Eng. 5, 8535–8540.

453   18.   Du, Y., Huang, Z., Wu, S., K., Xiong, X., Zhang, Zheng, B., Nadimicherla, R., Fu, R., and Wu, D.

454   (2018). Preparation of versatile yolk-shell nanoparticles with a precious metal yolk and a

455   microporous polymer shell for high-performance catalysts and antibacterial agents. Polymer. 137,

456   195–200.

457   19.   Zheng, X., Shen, G., Wang, C., Li, Y., Dunphy, D., Hasan, T., Brinker, C. J., and Su, B., (2017).

458   Bio-inspired Murray materials for mass transfer and activity. Nat. Commun. 8, 14921.

459   20.   Wang, X., Wang, X., Huang, Z., D., Miao, D., Miao, J., Zhao, J., Yu, and Ding, B. (2018).

460   Biomimetic fibrous Murray membranes with ultrafast water transport and evaporation for smart

461   moisture-wicking fabrics. ACS Nano. 13, 1060–1070.

462   21.   Adinata, D., Wan Daud, W. M. A. & Aroua, M. K. (2007). Preparation and characterization of

463   activated carbon from palm shell by chemical activation with K_2CO_3. Bioresour. Technol. 98, 145–

464   149.

465   22.   Dahal, N., García, S., Zhou, J. & Humphrey, S. M. (2012). Beneficial effects of microwave-

466   assisted heating versus conventional heating in noble metal nanoparticle synthesis. ACS Nano 6,

467   9433–9446.

468   23.   Wang, H. et al. (2012). Adsorption and desorption of mixtures of organic vapors on beaded

469   activated carbon. Environ. Sci. Technol. 46, 8341–8350.

470   24.   Lashaki, M. J. et al. (2012). Effect of adsorption and regeneration temperature on irreversible

471   adsorption of organic vapors on beaded activated carbon. Environ. Sci. Technol. 46, 4083–4090.

472   25.   Brunauer, S., Emmett, P. H. & Teller, E. (1938). Adsorption of gases in multimolecular layers. J.

473   Am. Chem. Soc. 60, 309–319.

474   26.   Jahandar Lashaki, M. et al. (2016). The role of beaded activated carbon's surface oxygen groups

475   on irreversible adsorption of organic vapors. J. Hazard. Mater. 317, 284–294.

476   27.   Pel, L., Valckenborg, R. M. E., Kopinga, K., Aarden, F. B. & Kerkhof, P. J. A. M. (2003).

477   Nitrobenzene adsorption in activated carbon as observed by NMR. AIChE J. 49, 232–236.

478   28.   Carter, G. T. et al. (2013). Mapping of functional groups in metal-organic frameworks. Science.

479   341, 882–886.

480   29.   Forse, A. C., Merlet, C., Allan, P. K., Humphreys, E. K., Griffin, J. M., Aslan, M., Zeiger, M.,

481   Presser, V., Gogotsi, Y., and C. P., Grey. (2015). New insights into the structure of nanoporous

482   carbons from NMR, Raman, and pair distribution function analysis. Chem. Mater. 27, 6848–6857.

483   30.   Deschamps, M., Gilbert, E., Azais, P., Raymundo-Piñero, E., Ammar, M. R., Simon, P., Massiot,

484   D.,and Béguin, F. (2013). Exploring electrolyte organization in supercapacitor electrodes with

485   solid-state NMR. Nat. Mater. 12, 351–358.

486   31.   Hippauf, F., Fulik, N., Hippauf, F., Leistenschneider, D., Paasch, S., Kaskel, S., Brunner, E., and

487   Borchardt, L. (2018). Electrolyte mobility in supercapacitor electrodes – solid state NMR studies

488   on hierarchical and narrow pore sized carbons. Energy Storage Mater. 12, 183–190.

489   32.   Schroeder, P. (1903). Uber Erstarrungs–und Quellungserscheinungen von Gela-tine. Z. Phys.

490   Chem. 45, 57.

491   33.   Román, S., Ledesma, B., Sabio, E., González, J. F. & González, C. M. (2016). Production of cost-

492   effective mesoporous materials from prawn shell hydrocarbonization. Nanoscale Res. Lett. 11, 435.

493   34.   Sun, Y., Wei, J., Wang, Y. S., Yang, G. & Zhang, J. P. (2010). Production of activated carbon by

494   K_2CO_3 activation treatment of cornstalk lignin and its performance in removing phenol and

495   subsequent bioregeneration. Environ. Technol. 31, 53–61.

496   35.   Chen, R., Li, L., Liu, Z., Liu, M., Wang C., Li, H., Ma, W., and Wang, S. (2017). Preparation and

497   characterization of activated carbons from tobacco stem by chemical activation. J. Air Waste

498   Manag. Assoc. 67, 713–724.

499   36.   Horvath, G. and Kawazoe, K. (1983). Method for calclualtion effective pore size distribution in

500   molecular sieve carbon. J. Chem. Eng. Japan 16, 470.

501   37.   Carrott, P. J. M., Carrott, M. M. L. R., Mourão, P. A. M. & Lima, R. P. (2004). Preparation of

502   activated carbons from cork by physical activation in carbon dioxide. Adsorpt. Sci. Technol. 21,

503   669–681.

504   38.   Foo, K. Y. & Hameed, B. H. (2012). Mesoporous activated carbon from wood sawdust by K_2CO_3

505   activation using microwave heating. Bioresour. Technol. 111, 425–432.

506   39.   Forse, A. C., Griffin, J. M., Merlet, C., Carretero-Gonzalez, J., Raji, A. R. O., Trease, N. M. and

507   Grey, C. P. (2017). Direct observation of ion dynamics in supercapacitor electrodes using in situ

508   diffusion NMR spectroscopy. Nat. Energy 2, 16216.

509   40.   Harris, R. K., Thompson, T. V., Norman, P. R. and Pottage, C. (1996). Adsorption competition

onto activated carbon, studied by magic-angle spinning NMR. J. Chem. Soc. - Faraday Trans. 92,

2615–2618.

41. Harris, R. K., Thompson, T. V., Norman, P. R. & Pottage, C. (1999). Phosphorus-31 NMR studies

of adsorption onto activated carbon. Carbon N. Y. 37, 1425–1430.

42. Devautour-vinot, S., Maurin, G., Serre, C., Horcajada, P., Cunha, D. P., Guillerm, V., Costa, E. S.,

Taulelle, F., and Martineau C. (2012). Structure and dynamics of the functionalized MOF type

UiO-66(Zr): NMR and dielectric relaxation spectroscopies coupled with DFT calculations. Chem.

Mater. 24, 2168–2177.

43. Anderson, R. J., McNicholas, T. P., Kleinhammes, A., Wang, A., Liu J., and Wu Y. (2010). NMR

Methods for characterizing the pore structures and hydrogen storage properties of microporous

carbons. J. Am. Chem. Soc. 132, 8618–8626.

44. Forse, A. C., Milner, P. J., Lee, J. H., Redfearn, H. N., Oktawiec, J., Siegelman, R. L., Martell, J.

D., Dinakar., L. B., Porter-Zasada, Gonzalez, M. I., et. al. (2018). Elucidating CO_2 chemisorption

in diamine-appended metal-organic frameworks. J. Am. Chem. Soc. 140, 18016–18031.

45. Valiollahi, S., Kavianpour, B., Raeissi, S. & Moshfeghian, M. (2016). A new Peng-Robinson

modification to enhance dew point estimations of natural gases. J. Nat. Gas Sci. Eng. 34, 1137–

1147.

46. Ania, C. O., Cabal, B., Parra, J. B., Arenillas, A., Arias, B., and Pis, J. J. (2008). Naphthalene

adsorption on activated carbons using solvents of different polarity. Adsorption 14, 343–355.

47. Vallieres, C., Winkelmann, D., Roizard., D., Favre, E., Scharfer, P., Kind, M., (2006). On

530   Schroeder's paradox. J. Memb. Sci. 278, 357–364.

531 48. Beers, K. M., Yakovlev, S., Jackson, A., Wang, X., Hexemer, A., Downing, K. H., and Balsara,

532   N.P. (2014). Absence of Schroeder's paradox in a nanostructured block copolymer electrolyte

533   membrane. J. Phys. Chem. B 118, 6785–6791.

534 49. Liu, X., Sun, C., Liu., H, Tan., W., Wang, W., Snape, C. (2019). Developing hierarchically ultra-

535   micro/mesoporous biocarbons for highly selective carbon dioxide adsorption. Chem. Eng. J. 361,

536   199–208.

537 50. Millward, A. R. and Yaghi, O. M. (2005). Metal-organic frameworks with exceptionally high

538   capacity for storage of carbon dioxide at room temperature. J. Am. Chem. Soc. 127, 17998–17999.

539 51. Forse, A. C., Griffin, J. M., Presser, V., Gogotsi, Y. and Grey, C. P. (2014). Ring current effects:

540   Factors affecting the NMR chemical shift of molecules adsorbed on porous carbons. J. Phys.

541   Chem. C. 118, 7508–7514.

542 52. Nandy, A., Forse, A. C., Witherspoon, V. J. and Reimer, J. A. (2018). NMR spectroscopy reveals

543   adsorbate binding sites in the metal-organic framework UiO-66(Zr). J. Phys. Chem. C. 122, 8295–

544   8305.

545 53. Aue, W. P., Bartholdi, E. and Ernst, R. R. (1976). Two-dimensional spectroscopy. Application to

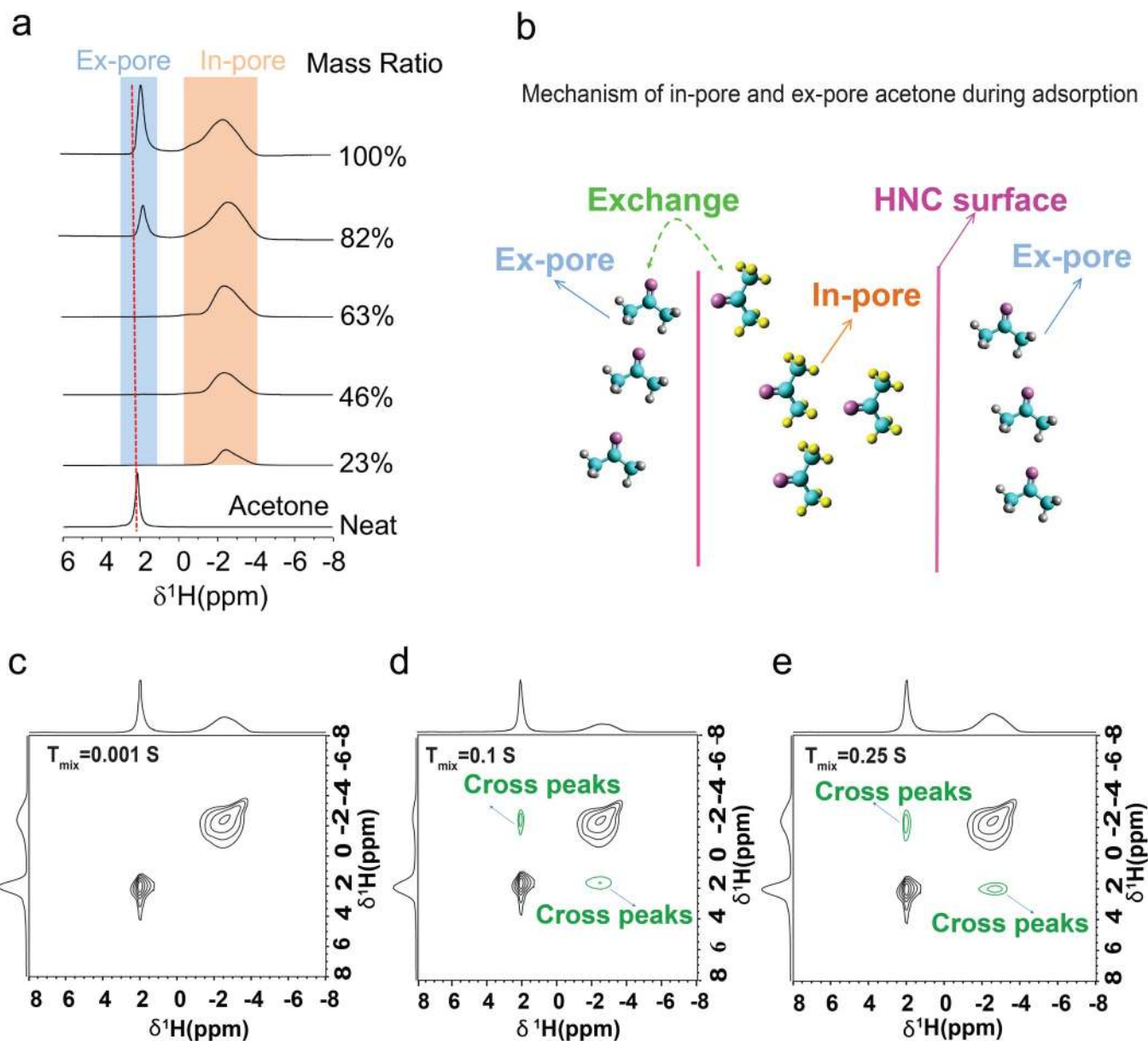546   nuclear magnetic resonance. J. Chem. Phys. 64, 2229–2246.

547

548 **Figures and Captions**

549
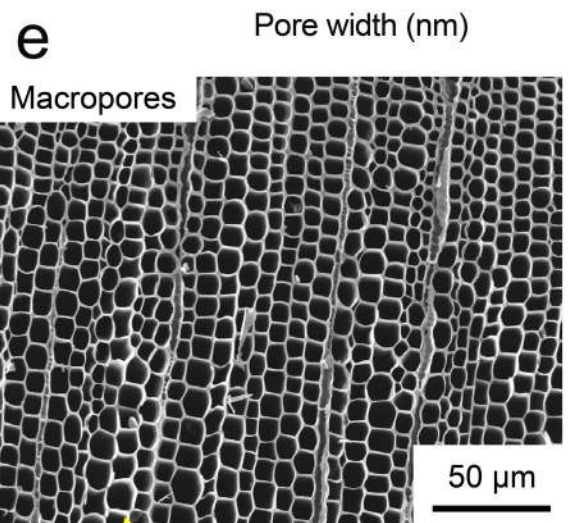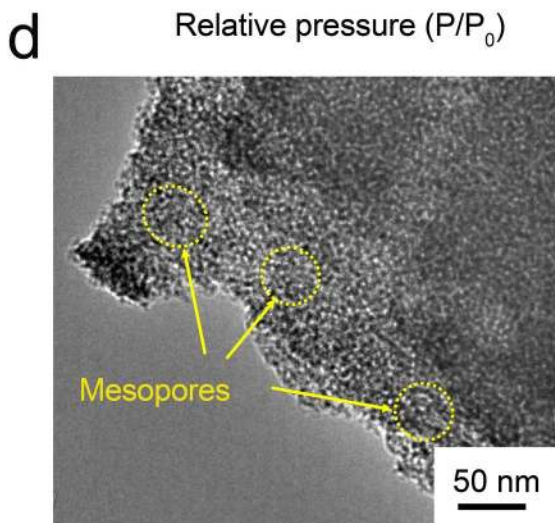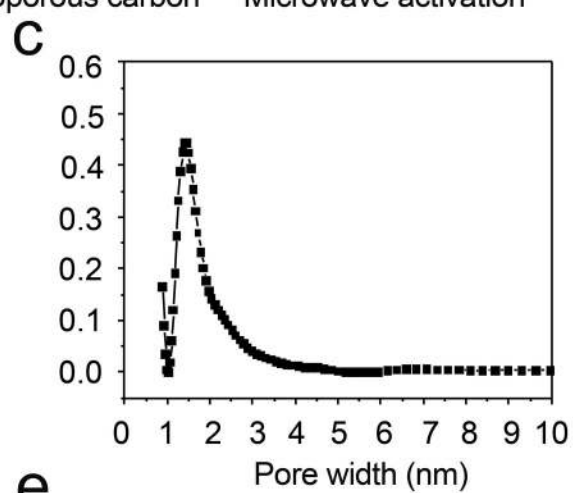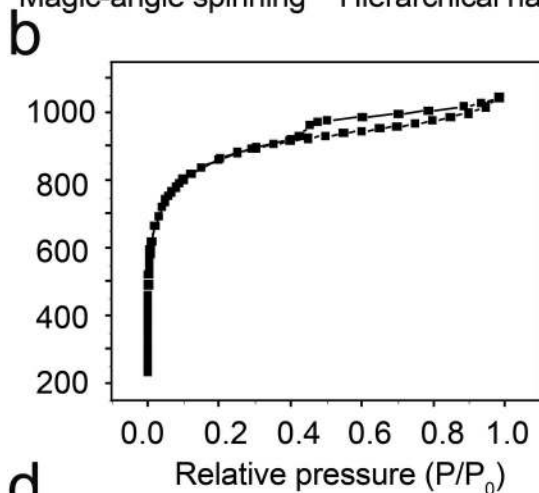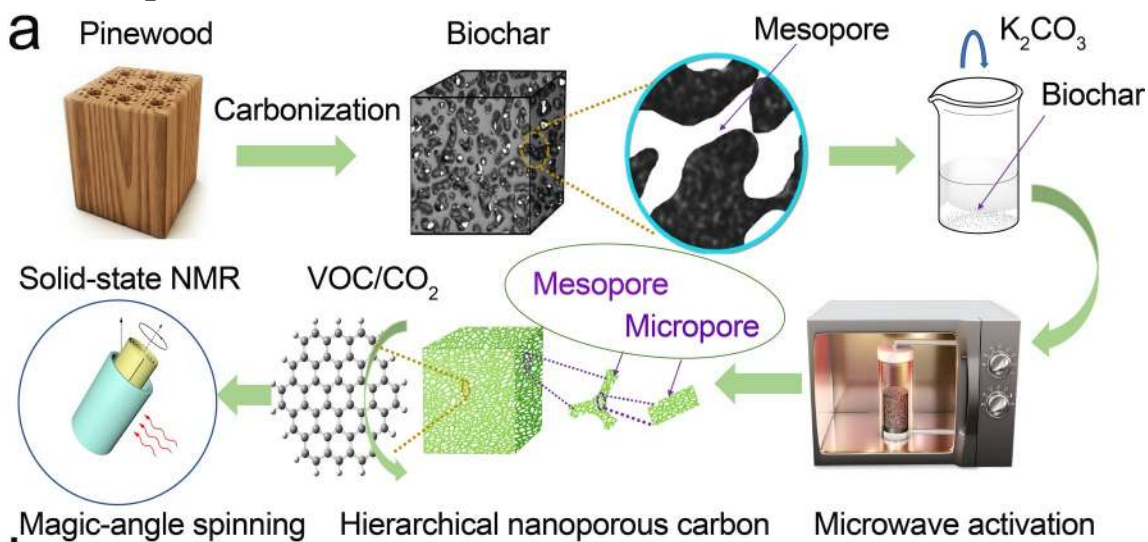
30

Figure 1 | Preparation and physical characterization of HNC. a, Schematic diagram of the fabrication process and characterization of the HNC; b. Ar adsorption isotherm at 77 K and c. pore size distribution of biochar and HNC; d, and e, TEM and SEM images of the HNC framework.


Figure 2 | Adsorption of liquid acetone in HNC by NMR. a, ^{1}H NMR spectra of acetone adsorbed onto HNC as a function of loading. The mass ratio is the (mass of acetone used/mass of hierarchical porous nanocarbon material). b, Scheme of the local environments of acetone molecules in HNC, including in-pore, ex-pore and exchange species; c, d, and e, 2D ^{1}H homonuclear correlation experiments. Experiments were performed on a sample with 100% mass ratio of (acetone/HNC), with mixing times of

559 0.001, 0.1 and 0.25 seconds, respectively. The cross peaks appearing at mixing times of 0.1 and 0.25 s
560 demonstrating slow exchange between in-pore and ex-pore environments.
561
562
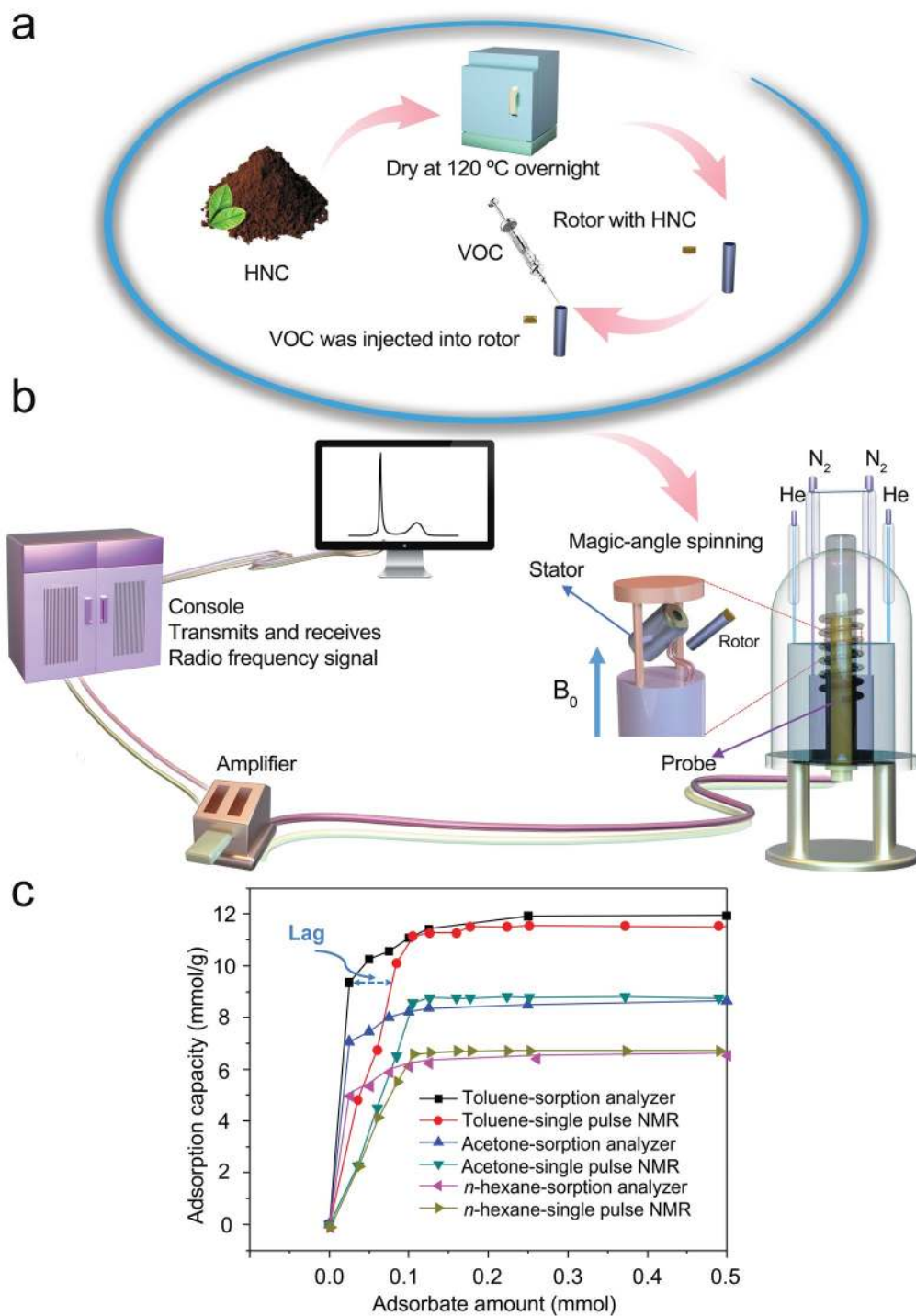
563

564 **Figure 3 | Uptakes of NMR and gas sorption data. a,** Schematic of the liquid VOC adsorption process;
565 **b,** Schematic of the solid-state NMR measurements of liquid VOC loaded HNC; **c,** Comparison of
566 uptakes between NMR data and gas sorption analyzer data for acetone, toluene and *n*-hexane loaded
567 hierarchical nanoporous carbon at room temperature (~298 K). NMR data corroborate the ultimate
568 adsorption capacity, but lag the isotherm data at low loadings.
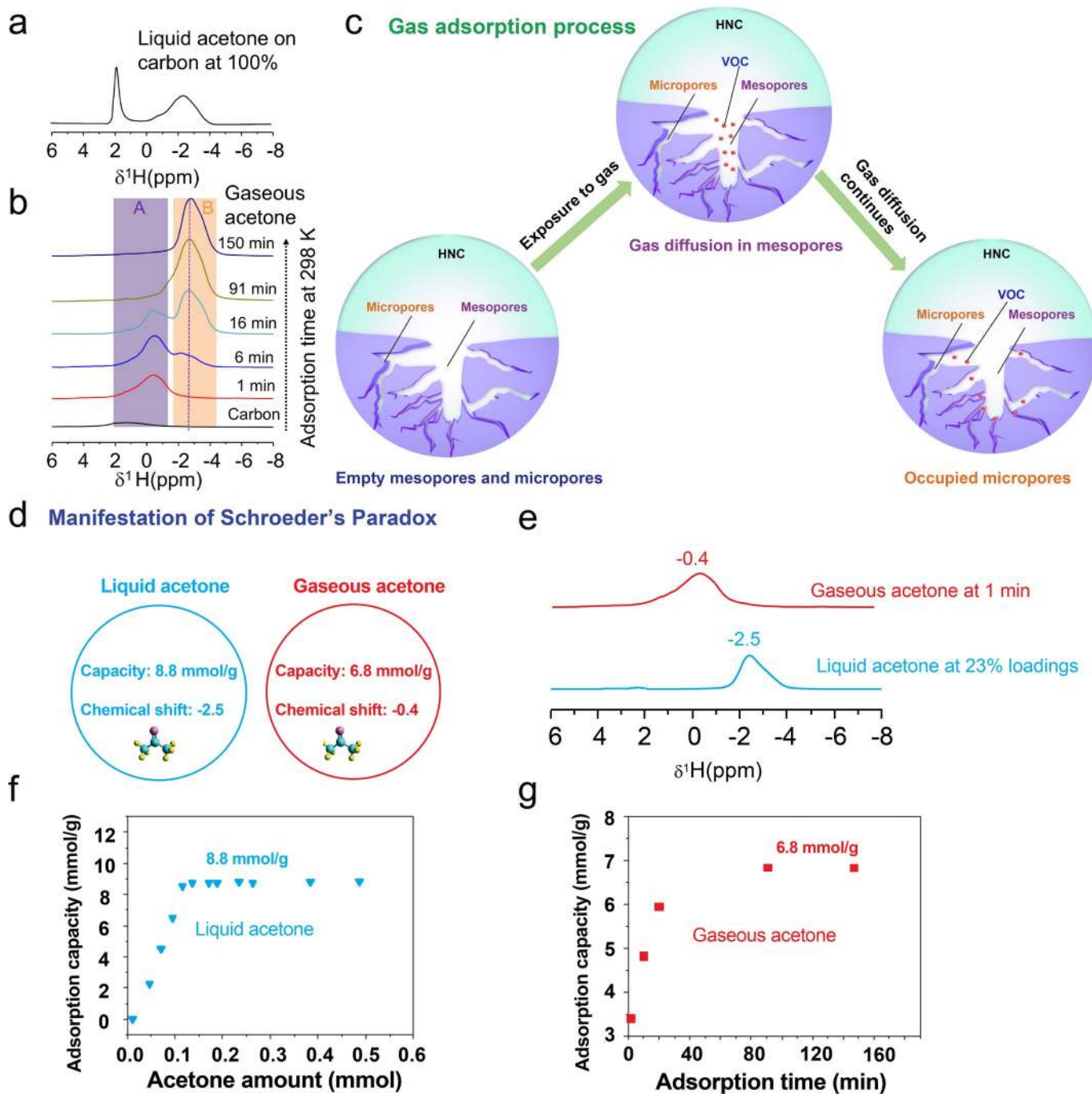
569

570 **Figure 4 | Vapor acetone adsorption mechanism and manifestation of Schroeder's Paradox onto**
571 **HNC. a,** ^{1}H NMR spectra of liquid acetone at 100 wt % loading is shown as a comparison; **b,** ^{1}H NMR

spectra of vapor acetone subject to HNC as a function of adsorption time at ~298K; **c,** Mechanism of vapor acetone adsorption process in different pores; **d ~ e,** Manifestation of Schroeder's Paradox on liquid and gaseous acetone adsorption capacity and chemical shift in HNC; **e,** Difference in chemical shifts; **f and g,** Difference in adsorption capacities; **(f,** The liquid acetone adsorption capacity at 100 wt %; **g,** The adsorption capacity ("A"+"B") changes with increase of adsorption time, and it reaches saturation over 91 min.)
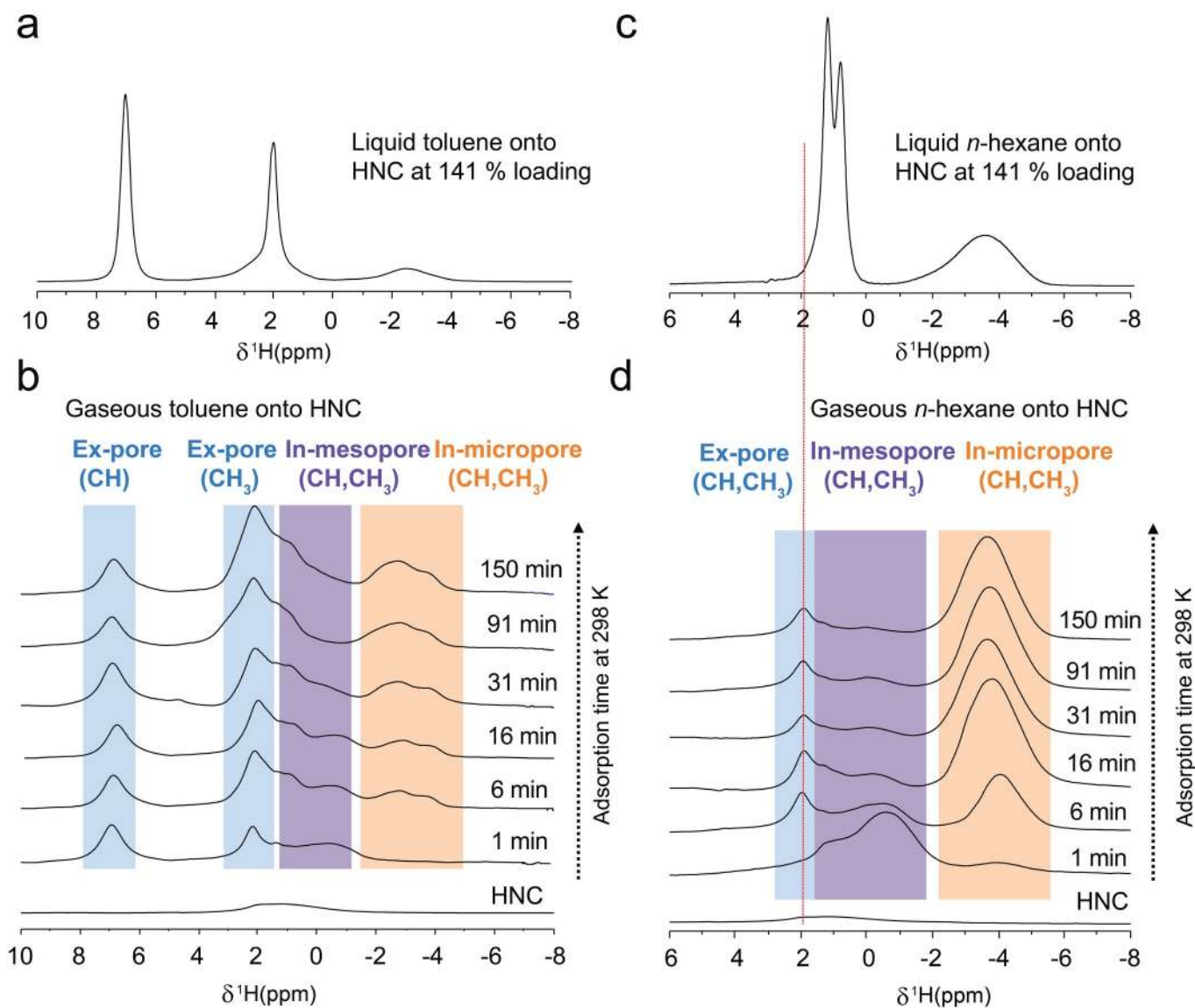
Figure 5 | Vapor toluene and *n*-hexane adsorption on hierarchical nanoporous carbon. a, ^{1}H NMR spectra of liquid toluene at 141 wt % loading is shown as a comparison; **c,** ^{1}H NMR spectra of liquid *n*-hexane at 141 wt % loading is shown as a comparison; **b,** ^{1}H NMR spectra of vapor toluene subject to HNC as a function of adsorption time; **d,** ^{1}H NMR spectra of vapor *n*-hexane subject to HNC as a function of adsorption time.

584
585
586
587
588
589
590
591

592
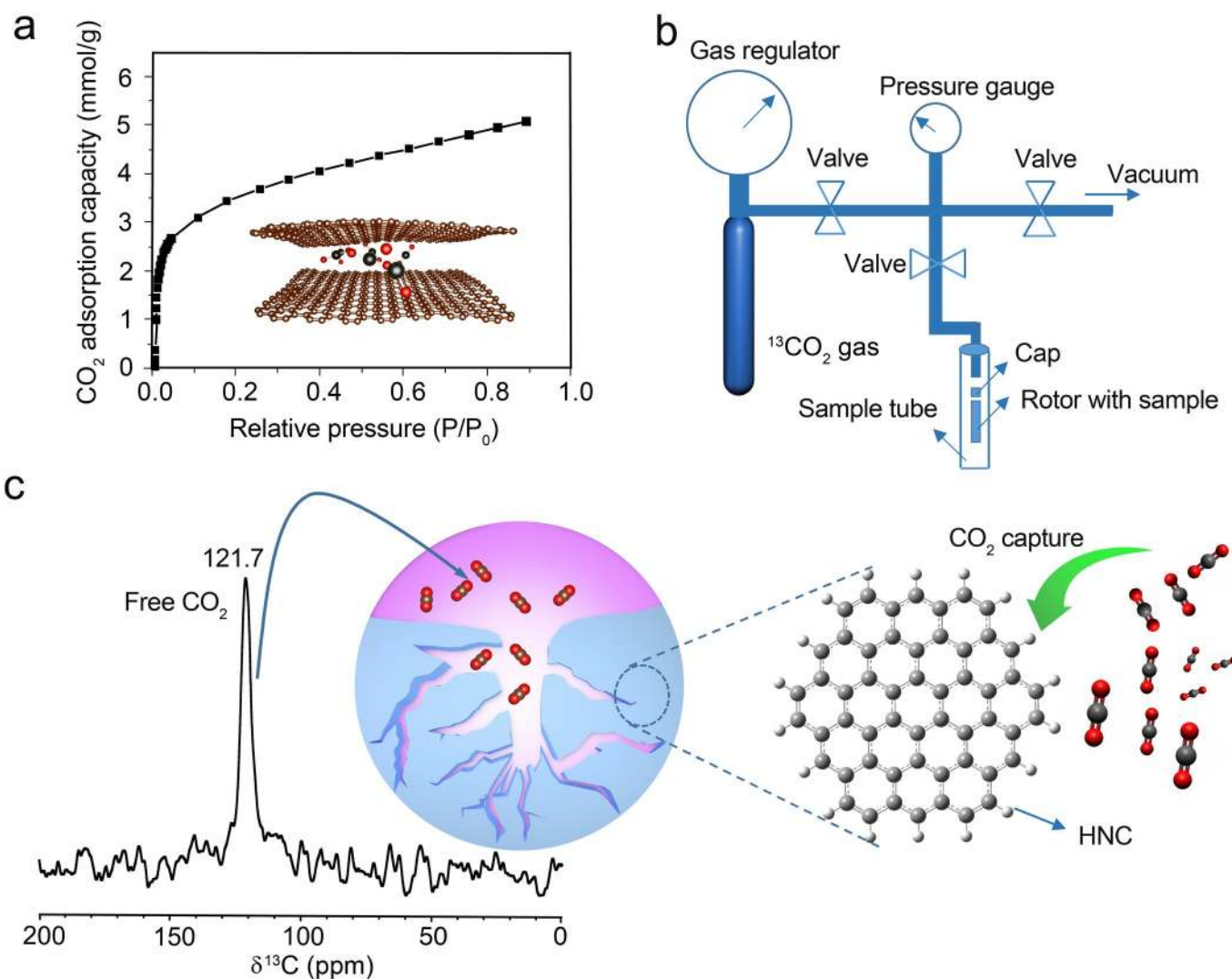
Figure 6 | CO$_2$ adsorption on hierarchical nanoporous carbon. a, CO$_2$ adsorption isotherm onto HNC at 298 K and 1 bar; adsorption isotherm samples were activated under N$_2$ at 120 °C for 2 h, followed by activation under vacuum at 120 °C for 4 h; **b,** Schematic of set up for CO$_2$ gas dosing into NMR samples; **c,** ^{13}C NMR spectra by direct excitation (no ^{1}H decoupling) on ^{13}CO$_2$ loaded HNC at 755 mbar.

597